EXPERIMENTAL INVESTIGATIONS OF ROTOR-FUSELAGE AERODYNAMIC INTERACTIONS USING A HELICOPTER POWERED MODEL

A. Le Pape*, J. Gatard+, J.-C. Monnier*

*Applied Aerodynamics Department
+Fauga-Mauzac Wind Tunnels Department
ONERA, BP 72, 92322 Châtillon Cedex, France

Abstract

This paper presents wind tunnel experiments of helicopter rotor-fuselage interactions. Several test campaigns have been conducted in the ONERA F1 subsonic wind tunnel on a Dauphin 365N model equipped with a powered main rotor. Numerous measurements have been performed during these tests: time-averaged and time-dependent fuselage pressure measurements, 6-components balance measurements, and Particle Image Velocimetry (PIV) measurements. This last technique allows to measure instantaneous velocity field in large planes around the helicopter for several blade positions along the rotor revolution. 2-components (2C) PIV results and 3-components (3C) stereoscopic PIV results are presented.

Each measurement technique accuracy and repeatability are first discussed, thanks to the large number of test points performed. The influence of the rotor downwash on the fuselage and the location of its impingement are then presented by analyzing the test points for different advance ratios and rotor thrust coefficients. The PIV results give finally a detailed description of the rotor wake in presence of the helicopter fuselage.

Notation

α	Fuselage incidence
β	Fuselage sideslip angle
Ω	Rotor rotation speed
R	Rotor radius
V_0	Freestream velocity
Q_0	Dynamic pressure
V_{tip}	Blade tip rotation velocity
$\mu=V_0/V_{tip}$	Advance ratio
ψ	Blade azimuth
c	Blade chord
S	Rotor surface
$\sigma=b.c/\pi.R$	Rotor solidity
ρ_∞	Density at infinity
β_0	Mean flapping angle
β_{1c}	Longitudinal flapping angle
β_{1s}	Lateral flapping angle
θ_0	Collective pitch angle
θ_{1c}	Lateral pitch angle
θ_{1s}	Longitudinal pitch angle
δ_0	Mean Lead-lag angle
δ_{1c}	1st harmonic (cosine term) of the lead-lag angle
δ_{1s}	1st harmonic (sine term) of the lead-lag angle
X	Axial force
Y	Side force
Z	Lift force
L	Roll moment
M	Pitching moment
N	Yaw moment
$Xbar=\frac{100.X}{\frac{1}{2}\rho_\infty S\sigma(R\Omega)^2}$	Axial force coefficient
$Ybar=\frac{100.Y}{\frac{1}{2}\rho_\infty S\sigma(R\Omega)^2}$	Side force coefficient
$Zbar=\frac{100.Z}{\frac{1}{2}\rho_\infty S\sigma(R\Omega)^2}$	Thrust coefficient
$Lbar=\frac{100.L}{\frac{1}{2}\rho_\infty S\sigma R(R\Omega)^2}$	Roll moment coefficient
$Mbar=\frac{100.M}{\frac{1}{2}\rho_\infty S\sigma R(R\Omega)^2}$	Pitching moment coefficient
$Nbar=\frac{100.N}{\frac{1}{2}\rho_\infty S\sigma R(R\Omega)^2}$	Yaw moment coefficient

Introduction

The flowfield around helicopters and especially rotor-fuselage interactions is of highest complexity and its understanding is of great interest to ensure good handling qualities and performance. Depending on the flight conditions, the rotor

downwash impinges the fuselage influencing both steady and unsteady aerodynamic loads, especially on the rear parts of the helicopter. Similarly, the fuselage has an influence on the rotor efficiency. The analysis of these interactions has been based upon both numerical and experimental studies for which most of the improvements performed in the computations of complex configurations of helicopter rely on detailed experimental database to ensure a relevant validation.

Since 1992, a realistic model of the Dauphin helicopter equipped with a powered main rotor was tested in ONERA S2Ch wind tunnel [1], [2] to study rotor-fuselage interactions. In addition to usual static and dynamic pressure transducers, numerous measurements techniques were used to characterize the flowfield: 5-hole probes, Laser Doppler Velocimetry (LDV), oil flow visualization. Other attempt of experimental database on helicopter rotor-fuselage interactions were done in the past: tests performed at NASA on the ROBIN fuselage [3] and tests performed by Leishman at the University of Maryland on a generic body shape [4], [5], [6]. But the Dauphin tests have the unequivalent particularity to be performed on a very detailed, realistic geometry, which has encouraged the further investigation of the flowfield around this model, in order to provide material for computation/experiment comparison as the complexity of the recent computations are about to reach the complete unsteady helicopter modeling [7], [8].

This paper presents new wind tunnel test entries of the ONERA Dauphin helicopter model that have recently been conducted in the F1 subsonic wind tunnel. The aim of these tests was to provide a further investigation of helicopter flowfield using the optical non-intrusive measurement technique: PIV (Particle Image Velocimetry). 2C and 3C PIV measurements synchronized with rotor positions along one revolution were thus performed in several planes around the helicopter body. The large amount of data gives a detailed experimental description of the rotor wake and its interaction with the fuselage; this is emphasized by the usual steady and unsteady pressure and loads measurements that were done simultaneously with PIV measurements.

After a brief description of the helicopter model, the wind tunnel and all the experimental measurement devices, a particular attention is devoted to the critical analysis of measurements accuracy and tests repeatability. The impingement of the rotor downwash on the fuselage is then discussed through the different measured data. In particular the influence of the flight conditions (advance ratio μ, and rotor thrust coefficient Zbar) is studied. Finally the PIV measurements are further analyzed to reach a detailed description of the characteristic of the rotor wake in the presence of the Dauphin fuselage.

Description of the experimental set-up

F1 subsonic Wind Tunnel

The experiments were conducted in the F1 subsonic wind tunnel. This facility is a close circuit pressurized wind tunnel with a rectangular test section size of 4.5 meters wide by 3.5 meters high. The wind tunnel is designed to perform tests with Mach numbers up to 0.36. In the present case, the tests were performed at an atmospheric stagnation pressure, and wind speed from 10m.s^{-1}, up to 30 m.s^{-1} corresponding to an advance ratio μ between 0.10 and 0.30, for a Reynolds number based on the fuselage length equal to 1.5 Million.

A view of the Dauphin model in the F1 wind tunnel test section is presented on Figure 1. No wall corrections are applied because of the small model size in comparison to the test section size.

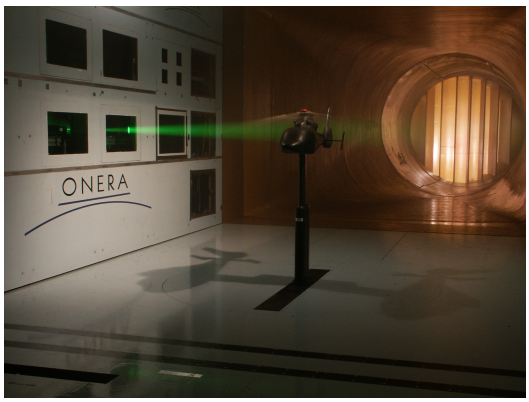

Figure 1: View of the Dauphin model in F1 wind tunnel

The Dauphin 365N model

The tested helicopter model is a 1/7.7 scale Dauphin 365N model equipped with a powered main rotor of 1.5m diameter. The four-bladed rotor is articulated in pitch, flap and lead-lag motions and the trim is obtained by collective and cyclic pitch angles by means of swashplate actuators, but no lead-lag damping devices are installed. The rotor shaft is tilted 4^{o} nose down. The blades are rectangular with a constant OA209 airfoil, a chord of 0.05m and a linear aerodynamic twist of -12^{o}/R. The rotor rotation is ensured by an electric engine in order to reach a blade tip speed RΩ=100 m/s. Consequently, the rotor is not Mach-scaled, the model being designed especially to study rotor-fuselage interactions at low advance ratios when compressibility effects are not that important.

The fuselage is 1.5m long; its shape is quite complex with slight simplifications in comparison of the real helicopter except for the fenestron that is not taken into account. Two different fuselages are used: one devoted to unsteady pressure measurements, equipped with 44 Kulite transducers (2 PSID range), and the other one devoted to steady pressure measurements, equipped with 234 steady pressure transducers (1 PSID range). The pressure transducers locations are presented on Figure 2.

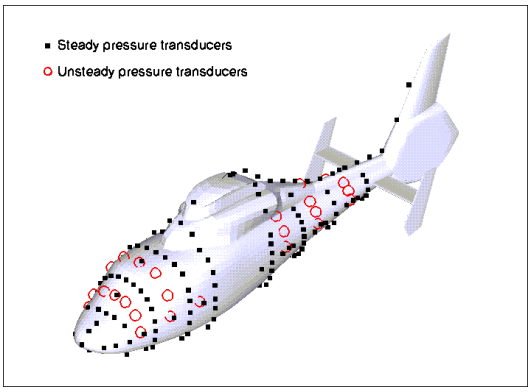

Figure 2: Position of steady and unsteady pressure transducers along the model fuselage

A 6-components balance is used to measure the global forces and moments acting on the fuselage and the rotor. This balance is placed inside the profiled strut that links the Dauphin model to the floor table which allows to vary the incidence and the sideslip angles (α and β) of the whole model with the strut.

Trim procedure and data acquisition

The control system of the rotor consists in a drive motor and electric control actuators which allow via a swashplate to control collective and cyclic pitch angles of the rotor. A test condition is defined by the orientation of the model with respect to freestream (incidence α and sideslip β), the advance ratio μ and the rotor thrust coefficient Zbar. In addition, the trim is done so that the global axial force acting on the model is zero (Xbar=0), and so that the lateral flapping angle is zero (β_{1s}=0).

For that purpose, static values of the rotor pitch, flap and lead-lag angles as well as their first harmonic values and the static values of forces and moments are measured. In addition, the acquisition is synchronized with the rotor rotation in order to measure the evolution of rotor angles and balance forces with the rotor revolution. 128 samples per revolution are acquired and averaged over 110 rotor revolutions.

PIV measurements set-up

Both 2C and 3C (stereoscopic) PIV measurements were performed in several planes (parallel and perpendicular to the freestream direction) around the helicopter model as shown on Figure 3. To achieve these measurements, two double cavity pulsed Nd-YAG lasers are used: they are located in the upper wall of the wind tunnel test section for the parallel planes (2x200mJ) or in the side wall for the perpendicular planes (2x150mJ) (see picture on Figure 1). Cameras (CCD, 1280x1024 pixels) are located in the wall of the test section. One camera is used for 2C PIV, and 2 cameras, one at each side of the plane, are used for 3C PIV. The time elapsed between two consecutive pictures depends on the freestream velocity and the plane position, with values between 50µs and 140µs. The laser beam and the camera recording are synchronized with the azimuthal blade positions. For each measurement plane, the PIV measurements have been performed for at least 32 azimuthal positions over one rotor revolution allowing to follow in detail the vortices emitted by each blade. Given the cadence of cameras shot and the laser pulsation frequency, a picture is taken every 8 rotor revolutions. Each final picture is the result of the averaging of 120 instantaneous picture acquisitions. The seeding is ensured by an olive oil diffuser placed downstream the test section.

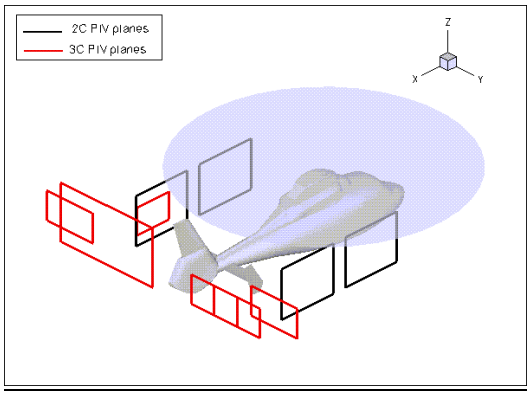

Figure 3: View of the PIV measurement planes around the helicopter model

The pictures are then analyzed using an intercorrelation technique on windows of 32x32 pixels size. More details about PIV measurements methods, and pictures post-processing techniques, especially for stereoscopic PIV can be found in [9], [10], [11], and[12].

Repeatability and accuracy of measurements

All along the different test campaigns, a particular attention has been paid to the control of the quality of the measurements and their reliability. The repeatability between test points in the same campaign or during different campaigns, but also the measurements accuracy was systematically checked.

Beyond the accuracy of the transducers themselves or the data acquisition devices range and sensitivity, a lot of uncertainties affects the measurements, such as the repeatability of the test conditions (rotor trim, wind speed), but also the natural unsteadiness of the flowfield due to the blade passages for example. The next paragraphs propose a brief critical analysis of each measurement techniques to evaluate the discrepancies due to the addition of measurement errors and repeatability errors.

Loads and moments measurements

For each test point, steady and unsteady loads and moments are measured using a 6-components balance. A statistical analysis has been performed on the static values of the loads on the fuselage and the rotor. For each test point, 120 samples measurements are performed, allowing to compute a mean value and the standard deviation σ of each component of the loads. Figure 4 shows the result of the statistical analysis for different test points performed during the four different test campaigns (from C1 to C4). The error bars on this figure represent the $[-3\sigma; +3\sigma]$ intervals which have been chosen as the confident intervals. It has to be noticed that the Xbar and Zbar values are the target, which define a given test condition.

During the same test campaign, the repeatability is in general satisfactory as the error bars are overlapping one with another. The repeatability between different test campaigns is also quite satisfactory except for the pitching and yawing moments for a few test points. The pitching moment Mbar measurement is indeed known to be very sensitive due to the impingement of the rotor downwash on the horizontal empennage of the helicopter for this test condition. The discrepancies remain limited and the repeatability for all forces and moments is good regarding the number of test points analyzed. This figure also shows the acceptable discrepancy of the targeted test point, Xbar and Zbar values are around their nominal values (0 for Xbar and 14.5 for Zbar).

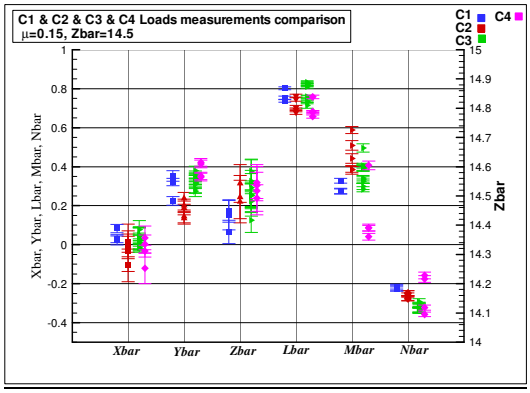

Figure 4: Statistical analysis of forces and moments measurements

Static pressure measurements

The Figure 5 shows the pressure distribution measured for the standard test conditions: μ=0.15, Zbar=14.5. Each Kp value is the mean of 50 measured test points, each tests points being averaged with 120 measurements. In addition the standard deviation σ of the measurements of these 50 test points has been computed for each transducer. The error bars on Figure 5 represent for each Kp measurement the $[-3\sigma ; +3\sigma]$ interval which has been chosen as the confident interval. Since these errors are based on the statistical analysis of a set of numerous test points, they integrate all the error sources: transducers accuracy, rotor trim repeatability, test conditions repeatability.

Given the very large amount of data taken into account, the steady pressure measurements accuracy is very good. The largest discrepancies are located behind the rotor hub, where a separation and consequently a strong unsteady flowfield is expected.

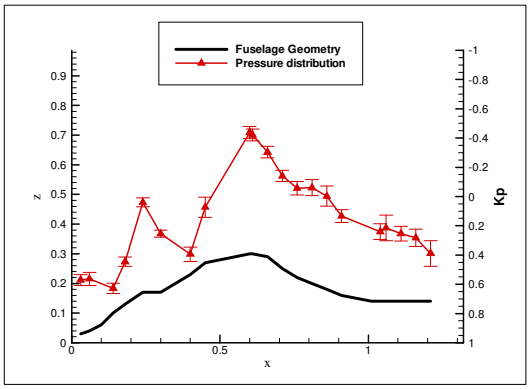

Figure 5: Steady pressure distribution measured along the upper longitudinal line of the Dauphin fuselage - μ=0.15, Zb=14.5

Dynamic pressure measurements

Only a few test points have been repeated in the case of dynamic pressure measurements which are heavier to carry out. It is reminded that each dynamic pressure measurement is done during 110 rotor revolutions and averaged, with 128 azimuthal samples over one rotor revolution.

Figure 6 shows the repeatability of dynamic pressure measurements located around the tail boom between a few test points. As mentioned previously, in addition to the influence of the rotor wake, a separation occurs in the area located behind the rotor hub. The repeatability of the time-accurate pressure measurements in this critical area is very good.

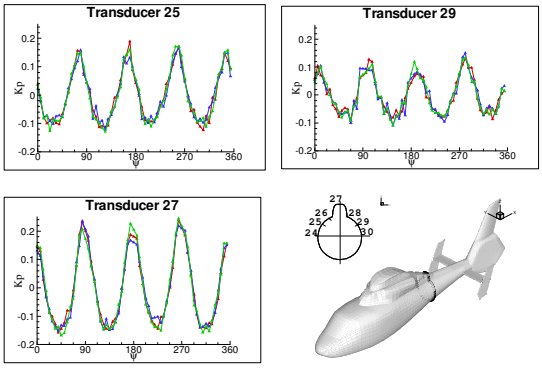

Figure 6: Repeatability of unsteady pressure measurements between 3 test points -μ=0.15, Zb=14.5

PIV measurements

Depending on the camera sensibility, the laser power, the intercorrelation methods, and the size of the analysis windows, an estimation of the measurement accuracy can be estimated. Details about such error estimation for PIV can be found in [13]. The point is here to evaluate the results accuracy and repeatability through a simple statistical analysis. As mentioned previously, each PIV picture is obtained by averaging 120 instantaneous pictures. The computations of the mean and the standard deviation of the vorticity over these instantaneous pictures are presented on Figure 7 (left). First one can notice that the most important discrepancies are located in and around the vortices. These discrepancies, illustrated by the standard deviation, represent on one hand the measurements errors, since the test conditions can be considered totally similar; the rotor has just done a few rotation and the total time of a full acquisition is around 2 minutes. On the other hand, these discrepancies can also be explained by the natural vortex wandering. It is indeed well known that the vortex are not exactly identical nor as their trajectories for the different blade passages and rotations. The values of the discrepancies remain significant: ~20m.s^{-2} for vorticity (~10%) and ~0.5 m.s^{-1} for velocity (~3%).

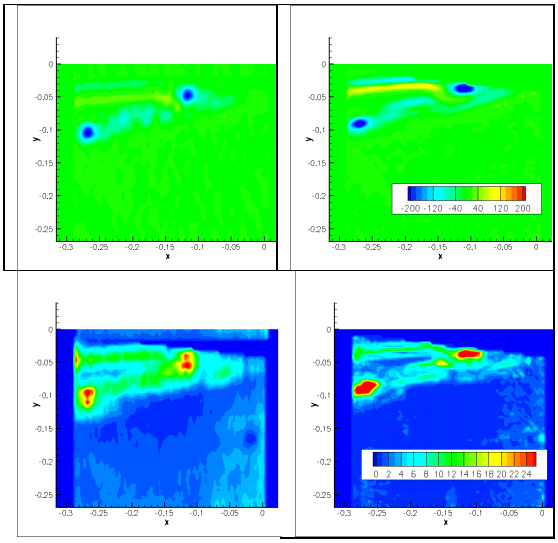

Figure 7: Mean (top) and standard deviation (bottom) of the measured vorticity by 2C PIV, based on 100 instantaneous pictures (left) and based on 10 repeated test points (right) -μ=0.15; Zb=14.5

In addition, for one given azimuthal position, some test points have been repeated. The repeatability of these final averaged PIV pictures has been analyzed (Figure 7 - right). In this case, the discrepancy is due to lack of repeatability of the test condition (rotor piloting, PIV plane, wind tunnel, etc…), since the 10 test points have been performed within several test days. The maximum discrepancies are still located in and around the vortices and are a slightly more important. The consequence is that the mean vortices shapes are not as round as for the instantaneous pictures. The measured position of the vortices is not exactly the same, probably because the rotor trim is not exactly the same.

This brief analysis of a set of 2C PIV data shows that the repeatability of the PIV measurements is acceptable, and gives an estimation of the measurement errors.

Rotor Downwash influence on the fuselage

Influence of advance ratio

A sweep in advance ratio has been performed for a fixed rotor thrust coefficient Zbar=14.5. Depending on the advance ratio, the rotor downwash is expected to be modified and its impingement location on the fuselage too. The higher the advance ratio is, the stronger the rotor

downwash is deflected. This is illustrated on Figure 8 which shows the static pressure distribution on the upper part of the fuselage. The effect of the rotor downwash can clearly be seen on the front part of the fuselage and behind the rotor hub and on the tail boom. This influence decreases with the increase of the advance ratio. For μ>0.20, the pressure distributions on the front and rear parts of the fuselage are quite similar, showing that the rotor downwash does not impinge the fuselage anymore.

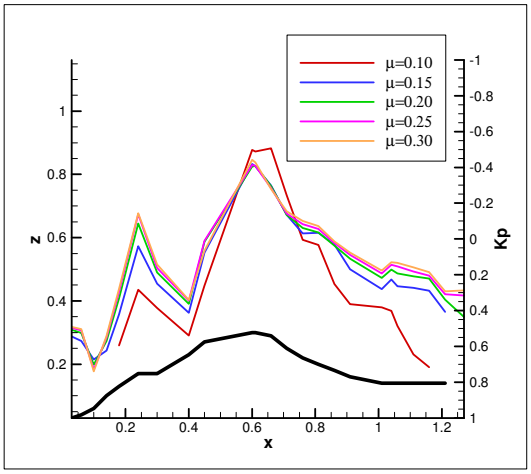

Figure 8: Steady pressure distribution on longitudinal upper line of the Dauphin fuselage for different advance ratio μ (Zbar=14.5)

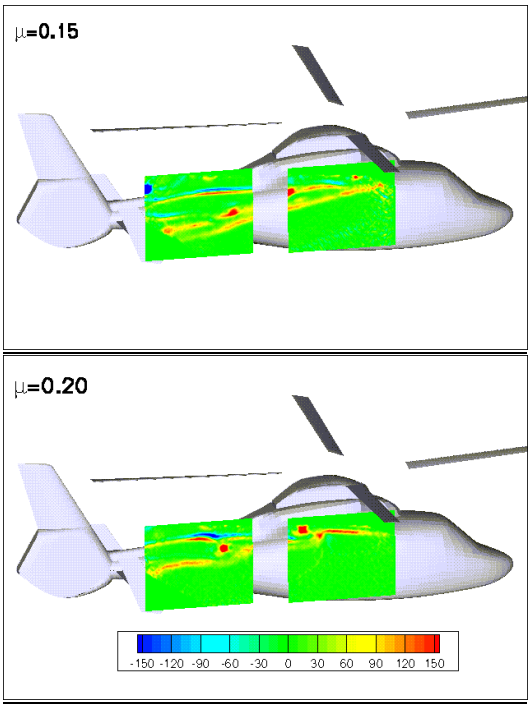

Figure 9: 2C PIV measurements for one azimuthal position on the retreating blade side – vorticity field

PIV measurements in longitudinal planes at r/R=0.66 (Figure 9) give a good representation of the rotor wake. The vortices emitted at each blade passage are clearly visible in addition to the shear layers. It is very clear that the downwards convection of the rotor wake structures (vortices and shear sheets) is more pronounced for μ=0.15 than for μ=0.20. The impingement of the rotor wake is thus located on the tail boom of the helicopter in the first case, and located more on the basis of the vertical fin in the second case.

The same kind of conclusions can be drawn from the analysis of unsteady pressure measurements, as shown on Figure 10. Values of the peak-to-peak pressure coefficient decrease with the high advance ratios, showing less rotor-fuselage interactions. In addition, the shape and the phase of the transducers response dominated by the 4/rev harmonic change with the advance ratio. Bi & Leishman have described several typical pressure signal signature for different steps of the rotor-fuselage interaction based on wind tunnel tests [4][5]. This typical pressure signal signatures can not be so clearly seen in our case, probably because of the much more complex shape of the Dauphin model in comparison of the one used by Bi & Leishman. Nevertheless, for high advance ratios the signal is close to the typical signature of a close body-wake interaction. The 4/rev harmonic is less important and the shape of the pressure signal becomes more and more disorganized.

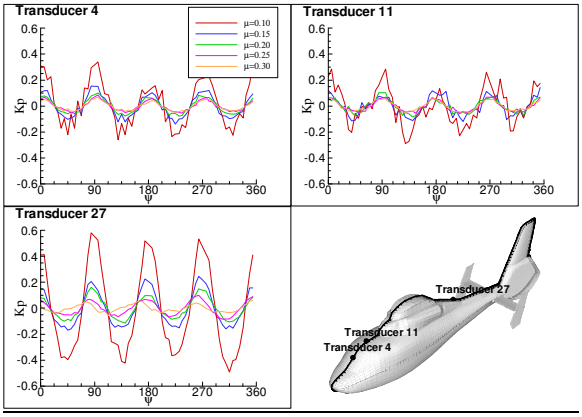

Figure 10: Fuselage unsteady pressure measurements on the upper longitudinal line for different advance ratios (Zbar=14.5)

This observation is confirmed by the analysis of the loads measurements and the pitching moment in particular as illustrated on Figure 11.

The pitching moment Mbar is strongly influenced by the aerodynamic loads on the rear part of the fuselage and in particular the horizontal empennage. As the pitching moment is positive for a nose-up motion, the mean values of Mbar (harmonic 0 in Figure 11) decrease from μ=0.1 to μ=0.2, when the rotor wake impingement with the rear part of the helicopter body is less important. A significant increase of Mbar is then observed for μ=0.3 and is not fully explained. The presence of a 1/rev component for every advance ratio indicates that the rotor is not perfectly equilibrated.

The evolution of the higher harmonics with the advance ratio gives additional information. For μ between 0.1 and 0.25, the pitching moment is dominated by the 4/rev component, showing the influence of the rotor wake and the blade passages. For μ=0.30, the 4/rev harmonic strongly falls and the higher 6/rev, 8/rev harmonics increase, which can also be seen on the time-evolution of the pitching moment Mbar on Figure 11. This indicates that at this advance ratio the rotor wake does not impinge the helicopter body anymore and the pitching moment is no more driven by blade passages.

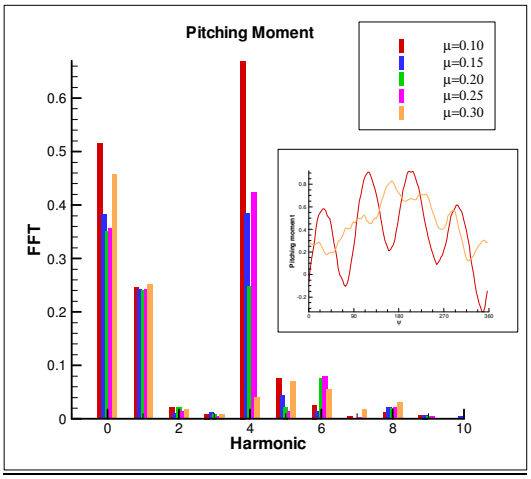

Figure 11: FFT of the measured pitching moment coefficients Mbar for different advance ratios

Influence of rotor thrust

Similar analysis can be made to study effect of the rotor thrust on the different types of measurements.

The static pressure coefficients along the top longitudinal line of the helicopter fuselage (Figure 12) show that higher the rotor thrust is, more pronounced the rotor downwash is. The influence is less visible than for the advance ratio because of the more limited scale of rotor thrust sweep (from Zbar=10 to 17.5).

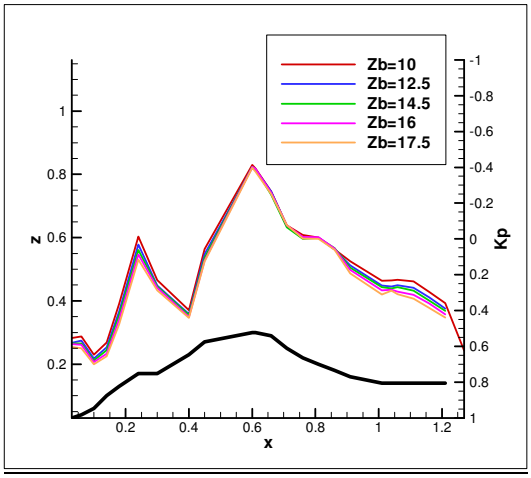

Figure 12: Steady pressure distribution on longitudinal upper line of the Dauphin fuselage for different thrust coefficients (μ=0.15)

The unsteady pressure coefficients comparison confirms the previous observation, and shows (Figure 13) that the influence of the rotor on the fuselage with the increase of the thrust coefficient is more important on the rear part of the helicopter. The shape of the Transducer 27 response for the highest thrust Zbar=17.5 is quite similar to the shape for smaller Zbar values, dominated by a 4/rev component. This shows that the rotor wake impingement still occurs at Zbar=17.5, and no near rotor wake –fuselage interaction is detected.

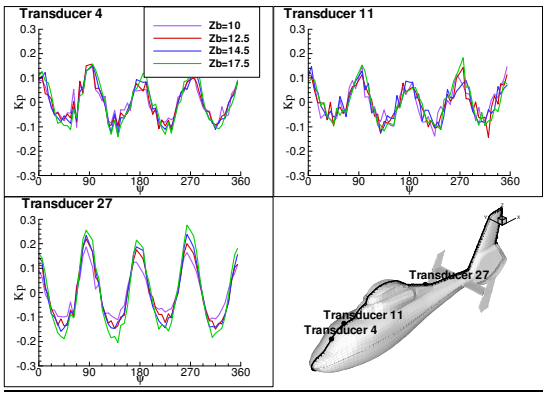

Figure 13: Fuselage unsteady pressure measurements on the upper longitudinal line for different thrust coefficients (μ=0.15)

Insight into rotor wake interaction with the fuselage

In this section the stereoscopic PIV data obtained in the planes perpendicular to the freestream and located just behind the helicopter fuselage are analyzed. The large size of the planes covering both the advancing blade side and the retreating blade side of the rotor and several instantaneous blades azimuthal positions allow a detailed description of the rotor wake and its interaction with the helicopter body.

In this part the analysis is focused on the standard test conditions: μ=0.15 and Zbar=14.5.

Time-averaged PIV results

First, the PIV results for the different rotor positions are time-averaged and compared to the previous data obtained in S2Ch with a five-hole probe (Figure 14), which are steady and averaged data. One can first mention that the longitudinal position of the measurement planes in the two wind tunnel were not exactly identical (x=0.63m behind the rotor centre for the S2Ch five-hole probe data, x=1.01m for the F1 PIV data). Nevertheless, the structures of the streamwise vorticity field are similar in both cases. Individual vortices remain visible on PIV measurement in F1 because the time-averaging is performed on a too few numbers of azimuthal positions over one rotor revolution. The good continuity of the PIV results through the different overlapping planes confirms a good repeatability of the test conditions and the PIV measurements.

Two main vortices of opposite signs appear on each side of the rotor corresponding to the edge vortices of the rotor disk. The shape of these vortices, and their history is detailed in the next section when analyzing the time-accurate PIV results.

One can also notice an area of positive vorticity on the advancing blade side of the rotor near the vertical empennage. The analysis of CFD computations (not shown here) indicates that this structure is not only due to the empennage wake but is also the consequence of the interaction of the inboard vortices emitted by the rotor with the rear part of the fuselage. The shape of this structure is in good agreement for both the measurement techniques.

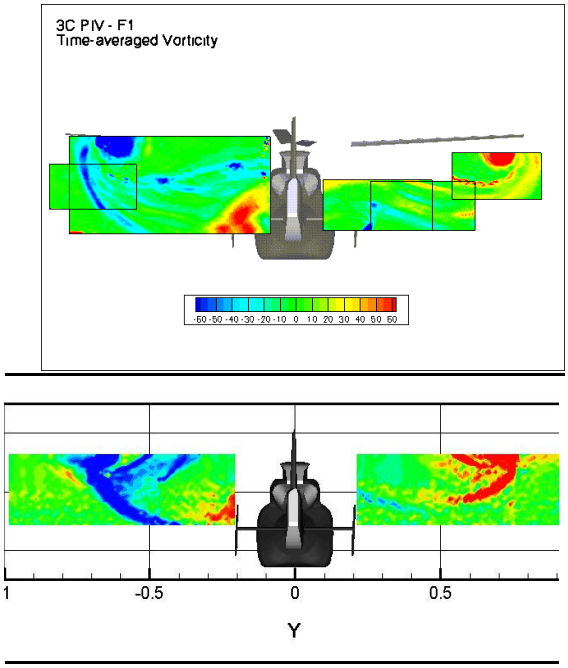

Figure 14: Time-averaged streamwise vorticity field - 3C PIV in F1 (top), five-hole probe in S2Ch (bottom)

Time-accurate stereoscopic PIV results

For each 3C PIV plane, at least 8 PIV measurements were performed corresponding to 8 azimuthal positions each 11.25° of rotor revolution (as a particular attention has been paid to ensure a perfect blade tracking, measurements are only necessary over one quarter of a rotor revolution). The final large amount of data allows to explore the evolution of the rotor wake and of its structures over a rotor revolution. This is illustrated by the different pictures of Figure 15 where the streamwise vorticity and streamwise velocity (third component of the stereoscopic PIV) are represented for different rotor positions.

Depending on the rotor position, the vorticity field lets several individual vortices appear (marked by the black circle on the advancing blade side of the top pictures as an example). These vortices are the blade-tip vortices emitted by each blade and that are convected downstream. The rolling up of these vortices takes place in opposite directions on the retreating blade side and the advancing blade side. Depending on the azimuthal positions of the rotor, one can notice the different positions of these blade-tip vortices. These traces of the vortices emission lines get from the inner part towards the outer part of the rotor wake and the vortices merge into the two main structures representing the global rotor disk edge vortices.

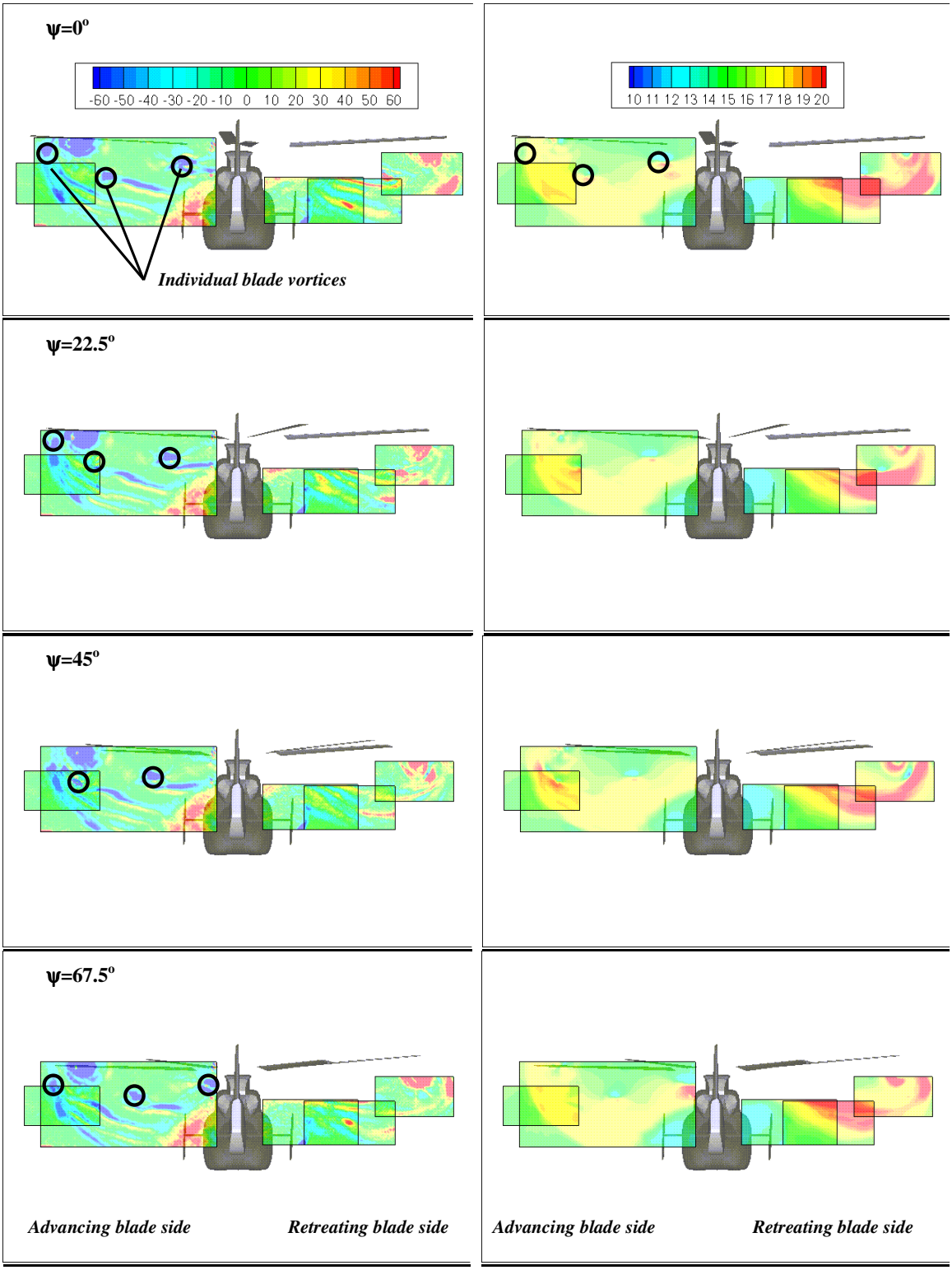

Figure 15: 3C PIV results in perpendicular planes to the freestream behind the helicopter fuselage for different rotor positions – Streamwise vorticity field (left) and normal velocity component (right)

These two mains structures are quite steady in comparison to the relative motion of the blade-tip vortices. One other steady structure can be observed: the positive vorticity area on the advancing blade side behind the vertical empennage described above.

Each vortex is associated with a shear layer that can be clearly seen on the pictures of Figure 15. The vorticity fields show also an alternation of shear layers of opposite signs. The same observations can be carried out when analyzing the 2C PIV results in the planes parallel to the freestream (see Figure 9 as an example); a succession of the blade-tip vortices and vortex sheets of opposite signs can be seen.

In general, a strong dissymmetry of the rotor wake between the advancing blade side and the retreating blade side is observed. Both streamwise vorticity and velocity fields show that the rotor wake deflection is more important on the advancing blade side as a consequence of the higher induced velocities, as illustrated on Figure 16 which present the computed induced velocity contours on the rotor disk. For that purpose, the comprehensive code HOST [14] developed by Eurocopter has been used. The streamwise velocity field (Figure 15 right) shows also a dissymmetry in the values of this component of the velocity. On the retreating blade side, the downward velocity is much more important. The individual blade vortices can also be seen on the streamwise velocity fields, the vortices being indeed associated with small distortion of the normal velocity.

At last, the small velocity components close to the helicopter fuselage and behind the vertical empennages show the extension of the fuselage wake at this location behind the helicopter body. The large influence of the fuselage wake on the rotor wake can be appreciated.

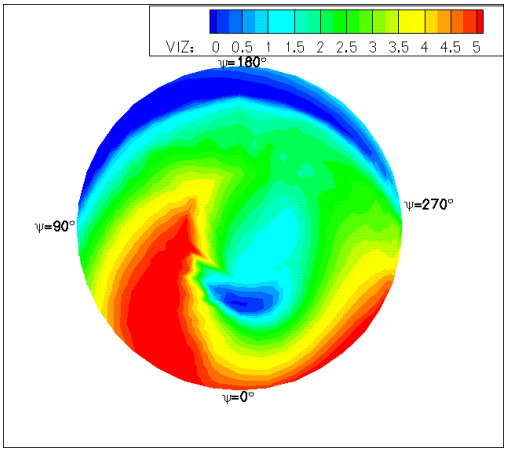

Figure 16: Induced velocity in the direction perpendicular to the rotor disk - computation with the lifting-line code HOST

Conclusion

A comprehensive experimental database about the aerodynamic interactions between a helicopter fuselage and its rotor has been presented. This database has been obtained over several wind tunnel test entries in the ONERA F1 subsonic wind tunnel, using a realistic Dauphin 365N helicopter shape model equipped with a powered and fully articulated main rotor. Different kinds of measurements have been performed: steady and unsteady fuselage pressure distributions, steady and unsteady loads and moments and rotor trim angles, and 2C and 3C Particle Image Velocimetry. These last measurements provide time-accurate data, the PIV pictures being synchronized with the rotor rotation.

The analysis of the accuracy and the repeatability of each measurement technique show the reliability of the wind tunnel tests. When possible, an evaluation of the discrepancies has been given. These discrepancies are for an important part due to the complexity of the test and especially the model piloting that involves difficulties to reach the wished test condition. Finally the analysis shows a good repeatability.

The combined analysis of the different measurements for numerous test conditions gives an overview of the rotor-fuselage interactions depending on the advance ratio and the rotor thrust. The influence of these parameters has been studied to determine the position of the rotor wake impingement on the helicopter fuselage, as the main feature of the interactions.

Finally, the rotor wake topology in presence of a fuselage is presented through the analysis of the stereoscopic time-accurate PIV measurements. Several vortex structures have been identified: the 3C PIV results show the individual blade-tip vortex rolling up in an edge disk vortex on the advancing and retreating blade sides. The stacks of vortex sheet (slice view of the helicoïdal rotor wake) are clearly visible. The global measured dissymmetric shape of the wake contains valuable information to compare and confront the computational results and deeply validate the CFD codes being developed at ONERA. Moreover, the analysis of the CFD computations results will probably help to understand the origin and the development of the structures highlighted by PIV results.

A large part of the presented database remains to be analyzed, in particular the 3C PIV measurements performed for a higher advance ratio. A new entry of the Dauphin model in the F1 wind tunnel is also envisaged in a near future to complement this unique experimental database.

Acknowledgment

The authors would like to thank all the wind tunnel people involved in these tests and the PIV team.

References

[1] Bettschart N., Gasser D.: *Analysis of helicopter rotor-fuselage interaction*, 20th European Rotorcraft Forum, Amsterdam (The Netherlands), October 1997

[2] Berry J., Bettschart N.: *Rotor-fuselage interaction: analysis and validation with experiment*, 53rd American Helicopter Society Forum, Virginia Beach (USA), 1997

[3] Mineck R., Gorton S.: *Steady and Periodic Pressure Measurements on a Generic Helicopter Fuselage Model in the Presence of a Rotor*, NASA/TM-2000-210286, June 2000

[4] Bi N., Leishman J.: *Experimental study on aerodynamic interactions between a rotor and a fuselage*, AIAA 7th Applied Aerodynamics Conference, Seattle, Washington, 1989

[5] Bi N., Leishman J., Crouse G.: *Investigation of rotor wake interactions with a body in low speed forward flight*, AIAA 9th Applied Aerodynamics Conference, Baltimore, MD, 1991

[6] Moedersheim E., Leishman J.: *Investigation of aerodynamic interactions between a rotor and t-tail empennage*, American Helicopter Society Specialist's Meeting, Stratford, Connecticut,1995

[7] Renaud T., Benoit C., Boniface J.-C., Gardarein P.: *Navier-Stokes computations of a complete helicopter configuration accounting for main and tail rotors effects*, 29th European Rotorcraft Forum, Friedrichshafen (Germany), September 2003

[8] Renaud T., O'Brien D., Smith M., Potsdam M.: *Evaluation of isolated fuselage and rotor-fuselage interaction using CFD*, 60th American Helicopter Society Forum, Baltimore (USA), June 2004

[9] Monnier J.-C., Gilliot A., Geilet C., Le Pape A.: *Caractérisation par PIV de l'interaction rotor-fuselage sur une maquette motorisée d'hélicoptère*, 9ème Congrès Francophone de Vélocimétrie Laser, Bruxelles, Septembre 2004

[10] Lawson N., Wu J.: *Three-dimensional particle image velocimetry: experimental error analysis of digital angular system*, Measurement Science and Technology, vol. 8, pp 1455-1464, (1997)

[11] Soloff S., Adrian R., Liu Z.-C.: *Distorsion compensation for generalised stereoscopic particle image velocimetry*, Measurement Science and Technology, vol. 8, pp 1441-1454, (1997)

[12] Willert C.: *Stereoscopic digital particle image velocimetry for application in wind tunnel flows*, Measurement Science and Technology, vol. 8, pp 1465-1479, (1997)

[13] Raffel M., Richard H., Ehrenfried K., Van der Wall B., Burley C., Beaumier P., McAlister K, Pengel K.: *Recording and evaluation methods of PIV investigations on a helicopter rotor model*, Experiments in Fluids, 36 (2004) pp 146-156

[14] Benoit B., Dequin A.-M., Kampa K., Grunhagen W., Basset P.-M., Gimonet B.: *HOST, A General Helicopter Simulation Tool for Germany and France*, American Helicopter Society, 56th Annual Forum, Virginia Beach (USA), May 2000